34th Symposium on Naval Hydrodynamics
Washington, D.C., June 26 – July 1, 2022

Effect of Surfactants on the Thermophysical Properties of Bubbly Water Systems and Bubble Collapse Dynamics Probed by Molecular Simulations

Jesse L. Prelesnik, Jingyi L. Chen, Mingning Zhu, Krishnan Mahesh, and J. Ilja Siepmann*
(University of Minnesota, Twin Cities, USA)

ABSTRACT

Naturally-occurring water sources tend to contain organic surfactants (Sabbaghzadeh *et al.*, 2017), which substantially alter the properties of the surface region. When bubbles are present, even small amounts of surfactant are sufficient to alter bubble dynamics, which must be included within the transport equations used for computational fluid dynamics (CFD) simulations of multi-phase flow (Muradoglu & Tryggvason, 2014). Molecular simulations are an ideal tool for investigating the validity of assumptions used in CFD because they consider the molecular nature of fluids explicitly, and physical observables such as surface tension are outputs rather than inputs (Chen *et al.*, 2019). The short temporal and spatial scales accessible to molecular simulations make them particularly well-suited to observing surfactant-influenced bubble collapse dynamics and the time scales of surfactant equilibration at liquid-vapor interfaces. This study utilizes molecular dynamics (MD) simulations of aqueous systems with pentan-3-ol as a representative surfactant, for which the time scales for surfactant equilibration between the liquid–vapor interface and the near surface region are found to be on the order of nanoseconds, $2-3$ orders of magnitude slower than time scales for collapse nanometer sized bubbles. Furthermore, the fast bubble collapse dynamics lead to additional surface-enrichment of surfactant and result in a nano-scale droplet consisting mostly of surfactant molecules that persists in solution several nanoseconds further. These findings differ from assumptions of instantaneous equilibrium included in numerous CFD models.

INTRODUCTION

Turbulent multi-phase flows are complex phenomena with a plethora of interrelated physicochemical driving forces that couple across large and small length and time scales (Bhatt & Mahesh, 2021; Schidmayer *et al.*, 2020). Predicting the behaviors of these flows is important for oceanographic engineering applications related to reducing noise and enhancing the longevity of naval vessels, but progress is hindered by an incomplete understanding of how the underlying processes couple (Luo *et al.*, 2016). At present, computational fluid dynamics (CFD) simulations are at the forefront of modeling multi-phase flows, and achieve this task by solving transport equations with source/drain terms. While a highly successful approach, effort is continually invested to improve the underlying physical model, including more detailed spatial variance of the input parameters and eliminating empiricism (Crowe, 2005; Yadigaroglu & Hewitt, 2017).

One route of providing this insight is via chemical simulations, in which molecular (particle) interactions are computed outright using first principles or representative force fields. The trajectories of particles through phase space can be used to evaluate via statistical-mechanical formalism their thermophysical properties, such surface tension or viscosity, but can also provide non-equilibrium properties with high spatiotemporal resolution. While this computation becomes intractable at macroscopic scales, including the particulate nature of matter explicitly accounts for interfacial effects without necessitating any assumptions about transport coefficients nor equations of state. These results can be compared with the Navier-Stokes hydrodynamics equations or other CFD frameworks, and permit a critical assessment of the validity of the underlying assumptions required therein. Furthermore, molecular simulations are able to probe model systems that are inaccessible experimentally, either due to resolution issues or mechanical instability at the bulk scale. Nano-bubbles are particularly interesting due to the knowledge gap surrounding them, owed to a deficiency

*Corresponding author, E-mail: siepmann@umn.edu

in experimental data and the increasing importance of molecular interactions that lead to deviations from planar interfaces.

This study emphasizes the role of small organic surfactants that occur naturally in seawater, and are known to localize to liquid-vapor interfaces (Sabbaghzadeh *et al.*, 2017). The presence of surfactant at the surface of a bubble alters the bubble's trajectory due to nonequilibrium surface tension gradients (Takagi & Matsumoto, 2011). These stresses can be sufficiently large to counteract shear-induced lift forces and the direction of bubble migration may be qualitatively incorrect without accounting for surfactant-induced stresses. An important question, then, is the rate at which surfactant molecules equilibrate between the bubble interface and bulk fluid, because this time scale determines which turbulent flow phenomena may be approximated as being at instantaneous equilibrium. This phenomenon is addressed from two sides: (1) Simulations with a thermodynamically stable bubble in which the initial surfactant distribution is nonequilibrium, to evaluate the time to equilibration; and (2) Bubble collapse simulations beginning from an appropriate initial surfactant distribution to examine the interplay between bubble radius and surfactant repartitioning.

Related problems have been addressed previously using classical molecular dynamics (MD) simulations. Prior works have assessed the conditions under which a bubble in neat water is thermodynamically stable, and established protocols for quantifying bubble size and sphericity, in addition to relevant thermodynamic properties (Chen *et al.*, 2019). Bubble collapse dynamics have also been investigated in the context on non-condensable gases and best practices have been presented (Siepmann *et al.*, 2020). This body of prior work has put forth trends associated with finite system size and choice of water model in both equilibrium and non-equilibrium properties. Here, we include pentan-3-ol as a representative surfactant as well. Pentan-3-ol is selected as surfactant because it offers a reasonably high-solubility limit that allows one to ensure that simulated systems with a reasonable of surfactants (to achieve good statistics) remain well below the saturation limit. The architecture of pentan-3-ol also results in each molecule occupying a large amount of interfacial area compared to the linear pentan-1-ol isomer. Previously, MD simulation studies have been used to provide a molecular-level description of collapsing nanobubbles (with and without the inclusion of nitrogen gas molecules), utilizing upwards of 10^6 particles. The inclusion of interfacial surfactant modifies the surface tension and gives rise to elongated collapse times, and leads to intense surfactant localization following collapse.

MODELS AND SIMULATION DETAILS

Two different types of particle-based models are used to describe water and pentan-3-ol in the MD simulations. The first type, called here MM, uses molecular-mechanics force fields where each molecule is represented by multiple interaction sites and where the intermolecular interactions are governed by pairwise-additive Lennard-Jones (LJ) and long-range Coulomb potentials. The second type are coarse-grain (CG) models that reduce the number of interaction sites and/or reduce the distance range for which energies and forces need to be computed. Here, we utilize the 4-site TIP4P/2005 water model (Abascal & Vega, 2005), which is known to accurately reproduce a variety of thermophysical properties under a wide range of conditions, such as shear viscosity, self-diffusion, and surface tension (Chen *et al.*, 2019). This water model is paired with the TraPPE–united atom (UA) alcohol model (Chen *et al.*, 2001), which was designed to reproduce bulk-phase coexistence curves for use in liquid mixtures. A combination of TIP4P water and TraPPE–UA for 1-butanol has also been shown to accurately predict their mutual solubility limit and the liquid–vapor surface tension for the two different saturated phases (Chen *et al.*, 2002). The TraPPE force field prescribes rigid bond lengths, which in this work are modeled as harmonic bonds using OPLS parameters as in prior MD studies (Kelkar, 2007; Campañá & Miller, 2013).

The CG model represents water as a single-site particle, called mW, which is able to capture the roughly tetrahedral structure of liquid water by using both pairwise-additive and three-body nonbonded potential energy terms that favor the necessary inter-particle angles (Molinero & Moore, 2009). The mW water model was paired with a united-atom pentan-3-ol model (Custer *et al.*, 2018) designed to mimic hydrogen-bonding with mW water via the same short-ranged potential energy function, and both molecules lack long-range electrostatics. While the second model (mW) reproduces water's thermophysical properties less accurately than the first (TIP4P/2005), the two models agree on many trends and correlations between these properties, and so both models can provide physical insight when observing deviations from bulk behavior. The mW model is particularly useful because of its short-ranged nature and reduction in number of interaction sites, allowing for larger simulations in both length and time.

MD simulations were conducted using the LAMMPS software package (Thompson *et al.*, 2022) from initial configurations generated by PACKMOL (Martínez *et al.*, 2009). For the MM model, the time step was 1 fs and both O−H bond lengths and H−O−H angles of water were constrained using the SHAKE algorithm (Ryckaert *et al.*, 1977). SHAKE was also applied to the alcohol O−H bond

length and C−O−H angle. Coulomb interactions were evaluated using a particle-particle particle-mesh Ewald solver with a tolerance of 10^{-5}, and Lorentz-Berthelot combining rules were applied to Lennard-Jones (LJ) interactions with a real-space and LJ cutoff parameter of 14 Å. For CG simulations, the time step was 5 fs. The water-water interactions are very short-ranged and decay to zero at a distance of approximately 1.5 times the hydrogen-bond distance (4.3065 Å). The accompanying surfactant hydrocarbon utilizes a 9-6 LJ potential with a cutoff of 10 Å. Depending on the system to be investigated, different MD simulation protocols were followed in this work.

The use of the CG models with the single-site description of water (i.e., fewer distances to be calculated), the shorter potential truncation, the lack of long-range electrostatic interactions, and the ability to use a larger time step allows one to access much larger system sizes than for the MM models. However, with present-day computing resources still restrict particle-based simulations with the CG models to linear dimensions only approaching 1 μm and simulation periods of less than 10 ns, i.e., no yet directly accessing the larger spatiotemporal scales probed by CFD.

Bulk Properties for Homogeneous Systems.

The simplest protocol is used here for homogeneous systems in the canonical (N_{water}, $N_{\text{surfactant}}$, V, T) ensemble at a temperature of 298 K with cubic box edge lengths of $L \approx 8$ nm, adjusted by 0−2% to give an average simulation pressure of 1 atm, as informed by supplementary simulations in the isobaric-isothermal ensemble (N_{water}, $N_{\text{surfactant}}$, p, T). The surfactant concentration was varied from 0 to a surfactant:water molar ratio of 1:160. For $N_{\text{water}} \approx$ 17,000, $N_{\text{surfactant}} \approx 110$. These simulations were allowed to relax for 2.5 ns before statistics were acquired for calculation of shear viscosities, η_{S}, over 20 ns. The shear viscosity was calculated with the Green-Kubo relation (Kubo, 1957),

$$\eta_{\text{S}} = \frac{V}{k_{\text{B}}T} \int_0^\infty \langle P_{\alpha\beta}(0) P_{\alpha\beta}(t) \rangle \mathrm{d}t, \tag{1}$$

where $P_{\alpha\beta}(0)$ and $P_{\alpha\beta}(t)$ are the off-diagonal components of the pressure tensor at times 0 and t, respectively, and η_{S} is averaged over the elements P_{xy}, P_{xz}, and P_{yz}. A time decomposition method was employed (Zhang *et al.*, 2015), using integral upper bounds specified in prior works (Chen *et al.*, 2019), to ensure adequate convergence. The shear viscosity was then converted to the kinematic viscosity ν_{S} by dividing by the total liquid density ρ.

Properties for the Planar Liquid–Vapor Interface

The second simulation protocol employed herein utilizes a slab geometry, also in the canonical ensemble, that includes a planar liquid-vapor interface. The dimensions of these simulations were $3 \times 3 \times 18$ nm^3, with ∼9 nm filled with liquid along the long (z) axis and the remaining space initially empty. Surfactant:water mole ratios of 1:160 (the same as in protocol one), and also 2:160, 3:160, and 4:160 were explored. For the CG model, an equilibration period of 40 ns allowed surfactants to appropriately aggregate at the surface before production runs of 40 ns. For the MM model, these times were 30 ns and 20 ns, respectively. After equilibrating surfactant molecules to the surface, the molecular density profiles along the z-axis were used to measure water and surfactant concentrations that allow us to compute the bulk fraction of surfactant from the regions separated by at least 2 nm from the interface.

The surface tension γ was then computed from the deviation between the normal and tangential components of the overall pressure tensor, a mechanical Kikwood-Buff route (Kirkwood & Buff, 1949),

$$\gamma = \frac{1}{2} \int_{-\infty}^{\infty} [P_{zz} - \frac{1}{2}(P_{xx} + P_{yy})] \mathrm{d}z, \tag{2}$$

where $P_{\lambda\lambda}$ is a diagonal component of the virial pressure, with $\lambda = x$, y, or z. Although a long-range correction to the Lennard-Jones potential can be applied for the planar interface (Vega & De Miguel, 2007), such a correction is not used here because it would not be applicable to two-phase flow systems. The planar surface tension computed this way for the MM and CG models fall slightly below the experimental value of ∼72 mJ/m^2 (Vargaftik *et al.*, 1983). Values of 65.4 mJ/m^2 and 65.9 ± 1.7 mJ/m^2 have been reported for the TIP4P/2005 (Vega & De Miguel, 2007; Chen *et al.*, 2019) (but note that the value would increase to 69.3 mJ/m^2 with tail corrections (Vega & De Miguel, 2007)). Tail corrections do not play a role for the short-range mW model, and the two reported values of 66.0 mJ/m^2 and 65.47 ± 0.24 mJ/m^2 are very consistent (Molinero & Moore, 2009; Chen *et al.*, 2019).

Properties of Thermodynamically Stable Bubbles

The third simulation protocol used here allows for (finite) simulations that contain a thermodynamically stable bubble with cubic box edge lengths of $L = 8$ or 16 nm (giving volumes of 512 and 4,096 nm^3, respectively). These simulations, too, were conducted in the canonical ensemble at $T = 298$ K. The molar ratio of surfactant to water was set to either 1:500 or 1:1,000, which is far lower than the experimental solubility limit. In each case the radius of the bubble R was chosen to be approximately $R/L = 0.15$. To achieve a thermodynamically stable bubble, the total system density needs to be significantly below the density of the saturated liquid phase and was set here using information from prior work for neat water (Chen *et al.*, 2019). Simulations were initialized from molecular configurations with a pre-formed bubble, a

spherical region of space centered in the simulation cell with an interior particle density of zero. A pre-determined fraction (0%, 10%, 20%, or 40%) of the total number of surfactant molecules present in a given system were initialy placed within 5 Å of the bubble surface. The quantity, $N_{\text{surfactant}}^{\text{interfacial}}/N_{\text{surfactant}}$, is denoted as the interfacial surfactant fraction. A brief pre-equilibration period of 250 ps was first conducted with a spherical wall in-place, allowing molecules to relax in the liquid region while the bubble volume and location remained fixed. This protocol is similar to that of Chen *et al.* (2019). The wall was then removed and the simulation allowed to proceed for 50 ns. During this production period, the number of surfactant molecules at the surface initially undergoes rapid increases or decreases (depending on whether the surface was initially under- or over-saturated), then gradually approaches the equilibrium value within a few nanoseconds, and fluctuates around this equilibrium value. The remainder of the simulation trajectory can then provide information on the equilibrium distribution.

When a thermodynamically stable bubble is present and the liquid-vapor interface is curved, eq. 2 is no longer applicable. In this case, the Young-Laplace (YL) equation is employed instead,

$$\gamma = \frac{1}{2} R(P_{\text{in}} - P_{\text{out}}), \tag{3}$$

where R is the bubble radius (as obtained from simulation using the algorithm described below), and P_{in} and P_{out} are the pressures inside and outside the bubble, respectively. The saturated vapor pressures of both water and pentan-3-ol are very small at 298 K, so we assume $P_{\text{in}} \approx 0$ and that P_{out} is the system total virial pressure.

Properties of Bubble Collapse

The final simulation protocol pertains to collapsing bubbles. Due to the supersonic speeds with which bubble collapse may occur and the associated local heating, the microcanonical (N_{water}, $N_{\text{surfactant}}$, V, E) ensemble is required to monitor collapse itself. In contrast to the case of thermodynamically stable bubbles, these microcanonical simulations used a total system density that is approaximately equal to the saturated liquid density. As in the preceding section, an initial pre-equilibration with spherical walls was conducted in the canonical ensemble at 298 K for 250 ps to relax the surrounding solvent without beginning the bubble collapse. The wall was then removed and a short relaxation period of 0.1 ps followed. Then, simulations were switched to the microcanonical ensemble and the bubble collapse timer began. While time steps of 5 fs can be used for the CG model near equilibrium, the violence with which bubble collapse occurs necessitates time steps of 2.5 fs to ensure energy conservation. With the MM model, a time step of 1 fs was used throughout. This protocol is similar to that of Siepmann *et al.* (2020), which investigated bubble collapse dynamics in the presence of a non-condensable gas.

The radius of a bubble during collapse can be compared against predictions provided by the Rayleigh-Plesset (RP) equation,

$$R\frac{\mathrm{d}^2R}{\mathrm{d}t^2} + \frac{3}{2}\left(\frac{\mathrm{d}R}{\mathrm{d}t}\right)^2 + \frac{4\nu_{\text{S}}}{R}\frac{\mathrm{d}R}{\mathrm{d}t} + \frac{2\gamma}{\rho R} + \frac{\Delta P(t)}{\rho} = 0 \tag{4}$$

where $\Delta P(t) = P_{\text{out}}(t) - P_{\text{in}}(t)$, as defined in the YL equation, was obtained from the actual simulation trajectory, but a cubic spline was used to smoothing the instantaneous pressure values. In solving the RP equation numerically for our test cases, the initial bubble radius $R(0)$ is provided. Furthermore, we assume that temporal variations in ρ, γ, and ν_{S} can be neglected. The relative change in ρ is small because the bubble occupies initially less than 1.5% of the system volume and, hence, the relative change in ν_{S} is also small. Since the surface coverage of surfactants and the bubble curvature are changing substantially during the bubble collapse process, the surface tension, γ, may also change. Thus, a given γ value may be viewed to some extent as a fitting parameter that approximates the temporal behavior over the trajectory. Nevertheless, a firm upper bound should be γ for the planar interface of neat water.

Determination of Bubble Volume, Sphericity, and Radius

The volume attributed to the bubble for a given molecular configuration was determined using a method described previously, in which Stillinger's cluster criterion (Stillinger, 1963) was used to compute the number of water molecule nearest neighbors, as defined by oxygen-oxygen (or site-site) distances less than or equal to 0.33 nm, as in Chen *et al.* (2019). Each water molecule is assigned as being liquid-like if it has two or more nearest neighbors, and vapor-like otherwise. The simulation box is then divided into a fine mesh with cubic voxels of edge length 0.2 nm and each cell is qualified as liquid-like if it contains a liquid-like molecule or if its center is within 0.33 nm of at least two liquid-like molecules, and the cell is vapor-like otherwise. Vapor-like cells are then clustered together if they share at least one corner, and the largest cluster is taken to be the bubble. Since transient voids appear even in bulk liquid water, a cutoff value is needed to distinguish whether a collapsing bubble's size is distinguishable from background noise. That cutoff is here taken to be 10 voxels, or 0.08 nm^3. This same algorithm is extended to include all atom types in the system, rather than only water, which is particularly relevant for describing surfactant-enriched bubble collapse, which leads to a nano-scale droplet consisting of mostly surfactant molecules after the vacuous bubble has vanished.

Bubble sphericity was evaluated using the three eigenvalues of the diagonalized gyration tensor, λ_1, λ_2, and λ_3, which give the relative shape anisotropy κ via the relation,

$$\kappa = 1 - 3\frac{\lambda_1\lambda_2 + \lambda_2\lambda_3 + \lambda_1\lambda_3}{(\lambda_1 + \lambda_2 + \lambda_3)^2}, \quad (5)$$

which attains a minimum value of 0 for a spherically symmetric shape and a maximum of 1 for a linear shape. Prior works suggest that nanobubbles tend to be highly spherical, an observation reproduced herein, and therefore the radius of the bubble can be determined from its volume, $R = (3V_{\text{cell}}/4\pi)^{1/3}$. This computation agrees well with the location of the Gibbs dividing surface as determined by fitting radial density profiles to a hyperbolic tangent function (Chen *et al.*, 2019).

RESULTS

Effects of Surfactant on Equilibrium Properties

The kinematic viscosity of an isotropic solution is found to increase by upwards of 10% in the highest surfactant conditions examined compared to neat water, increasing from 3.17 to 3.6×10^{-7} m^2/s for the CG model. Values obtained in neat water are quantitatively in-line with prior simulation studies using these models (Chen *et al.*, 2019), and the increase in mixture viscosity is expected based upon empirical relations such the Grunberg-Nissan equation (Grunberg, 1958). These viscosities will serve as parameters for the RP equation to model bubble collapse.

Table 1: Simulation details for homogeneous systems of box length $L = 8$ nm containing water and surfactant in a prescribed molar ratio, and the corresponding virial pressures and measured viscosities.

Composition (surfactant:water)	Density (kg/m^3)	Pressure (MPa)	Viscosity (10^{-7} m^2/s)
CG[a], 0:1	998.3	0.0 ± 0.1	3.17 ± 0.04
MM[a], 0:1	995.2	3.40 ± 0.09	8.8 ± 0.4
CG, 1:160	999.5	0.1 ± 0.2	3.6 ± 0.2
MM, 1:160	993.3	0.1 ± 0.1	9.0 ± 0.3

[a] From Chen *et al.* (2019).

The preferential adsorption of pentan-3-ol at the liquid–vapor interface leads to a concurrent depletion in the remainder of the finite simulated system. At the highest total surfactant:water ratio of 1:40.7 (total mole fraction of 2.40×10^{-2}), the equilibrium mole fraction in the bulk region is reduced to $(2.9 \pm 0.3) \times 10^{-3}$. The tendency for preferential adsorption diminishes as the surface gets crowded. The data presented in Figure 1 indicate that the preference for interfacial adsorption is significantly more pronounced for the MM model because the values for the bulk fraction of pentan-3-ol are shifted to lower values campared to the CG model for simulations using the same overall surfactant:water ratio. Due to the stronger surface adsorption preference, as described by the Gibbs adsorption equation, the MM model also yields a lower surface tension than the CG model.

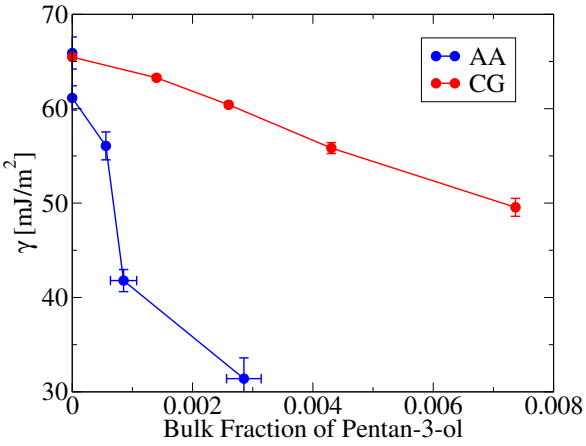

Figure 1: Surface tension γ as a function of the pentan-3-ol mole fraction in the bulk phase for the CG model (red) and the MM model (blue) with their respective surfactants. Uncertainty estimates are smaller for the CG model due to longer simulation trajectories.

For the total surfactant:water ratios investigated here, the surface tension decreases by more than 30 and 50% for the CG and MM models, respectively. While these values of the surface tension may be provided as input parameters to numerical solutions of the RP equation, it is worth noting that these computed surface tension values were obtained at equilibrium. In contrast, during bubble collapse the innermost shell of liquid becomes composed almost entirely of surfactant (see below). Furthermore, these equilibrium values correspond to planar interfaces, which at nanoscopic length scales are different than convex curved interfaces, and it remains an open question whether strong local curvature would lead to a change in surface tension for equivalent surfactant coverage.

Surfactant Distributions Around Stable Bubbles

While the bulk region is easily defined by considering volumes > 2 nm away from the putative interface, a definition of the interfacial region itself requires a density analysis. The density profile of water $\rho_{\text{liq}}(z)$ at the vapor-liquid interface, planar or curved, is known to transition smoothly from low to high sigmoidally, and may be fitted with a hyperbolic tangent function to obtain an

estimate of the interfacial width (Cahn & Hilliard, 1958).

$$\rho_w(r) = \frac{1}{2}(\rho_{liq} + \rho_{vap}) + \frac{1}{2}(\rho_{liq} - \rho_{vap})\tanh\frac{2(r-r_0)}{d}, \quad (6)$$

where ρ_{liq} and ρ_{vap} are the fitted densities in the liquid and vapor phases, respectively, r_0 is the position of the interface, and d is its thickness. When surfactant is present, the shape of the density profile $\rho_s(r)$ changes qualitatively and a pronounced peak appears near $r \approx r_0$ (see Figure 2). We find that this peak is well-captured by adding a Gaussian term to eq. 6 with centroid r_1 and variance σ^2 (standard deviation σ).

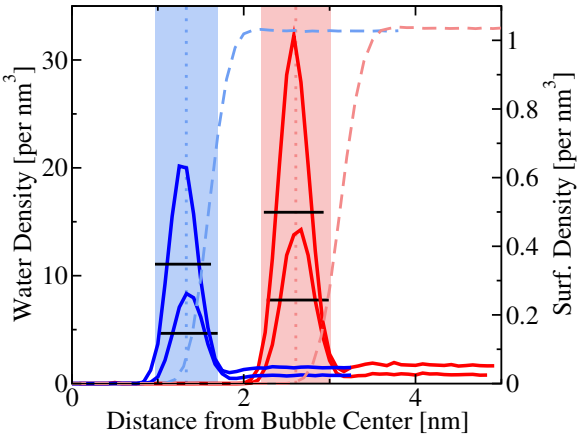

Figure 2: Number density profiles of CG water, $\rho_w(r)$, dashed lines, and pentan-3-ol, $\rho_s(r)$, solid lines, at equilibrium as a function of distance from the center of a thermodynamically stable bubble with $R/L \approx 0.15$ for $L = 8$ (blue) and $L = 16$ nm (red). Two traces are shown for $\rho_s(r)$ at both size scales, the taller of which corresponding to an overall 1:500 surfactant:water molar ratio and the shorter to 1:1,000. The corresponding mole fractions of surfactant in the bulk region are $(8.2 \pm 0.4) \times 10^{-4}$ ($L =$ 16 nm, 1:1,000); $(1.2 \pm 0.3) \times 10^{-3}$ ($L = 16$ nm, 1:500); $(5 \pm 2) \times 10^{-4}$ ($L = 8$ nm, 1:1,000); and $(1.4 \pm 0.3) \times 10^{-3}$ ($L = 8$ nm, 1:500), where uncertainty estimates are the standard error of the mean over four replicate simulations. Shaded regions correspond to $r_0 \pm d$ from eq. 6, and horizontal black bars show the width $r_1 \pm 2\sigma$.

From this density profile the concentration of surfactant at the interface can be estimated by summing over surfactant molecules within 2σ of position r_1, which amounts to ~95% of the area of a Gaussian. This definition of interfacial surfactant is comparable to integrating from $r_0 - d$ to $r_0 + d$ defined by the water molecules, as seen in Figure 2 for thermodynamically stable bubbles at equilibrium.

A finite-size/curvature effect is observed for the CG model when comparing thermodynamically stable bubbles with $L = 8$ and 16 nm and $R/L \approx 0.15$, where the extent of interfacial surfactant adsorption is diminished around bubbles of smaller radii (see Figure 2, comparing red and blue solid traces). This effect persists as the bulk surfactant concentration is varied by a factor of ~ 2. This is attributed to tight curvatures being more geometrically compatible with water hydrogen bond networks, leading to a higher energetic barrier for surfactant molecules to disrupt the interfacial water (Chandler, 2005).

When thermodynamically stable bubbles are initialized from non-equilibrium distributions of surfactant molecules, the time it takes to approach steady-state may be on the order of nanoseconds. This is determined by monitoring the bubble radius and fraction of surfactant molecules at the interface over time. In the most extreme conditions studied here, where at time $t = 0$ the interfacial surfactant fraction is either 0 or 0.4, the equilibrium value of 0.20 ± 0.01 is approached approximately exponentially, with time constants of 3.3 ± 0.1 and 4.1 ± 0.2 ns, respectively (see Figure 3, Top).

The re-distribution of surfactants between the bubble interface and the bulk liquid also results in changes of the bubble radius. However caution is required because interfacial surfactant molecules can be viewed either as part of the liquid or as part of the bubble. For the analysis shown in Figure 3, the bubble is detected considering only the location of water molecules. For the red trace for which the surface is initially supersaturated with surfactant molecules, we observe that the bubble radius decreases. Although one may initially surmise that the bubble volume decreases because the surface tension increases as surfactants are lost, this does not appear to be the main reason (see below). The larger contribution comes from the increase in the number of surfactants in the liquid region that, with their partial molar volume, lead to a swelling of the liquid region. The approach to equilibrium for the bubble radius is also well described by an exponential decay (with time constants 5.5 ± 0.5 and 6.2 ± 0.6 ns, see Figure 3, Middle). While an increasing/decreasing surface concentration of pentan-3-ol should lead to a change in opposite direction for the surface tension, this effect could not be quantified during the approach toward equilibrium. Since changes in R are relatively small, computing γ via the YL equation is largely dependent on P_{out}, which fluctuates wildly over small times. At equilibrium, the average $\langle P_{out} \rangle$ is well-defined, but is insufficiently converged on small time scales even with multiple simulation replicas.

Bubble Collapse Dynamics with Surfactant

While the equilibration time for re-distribution of surfactants between the interface and the surrounding

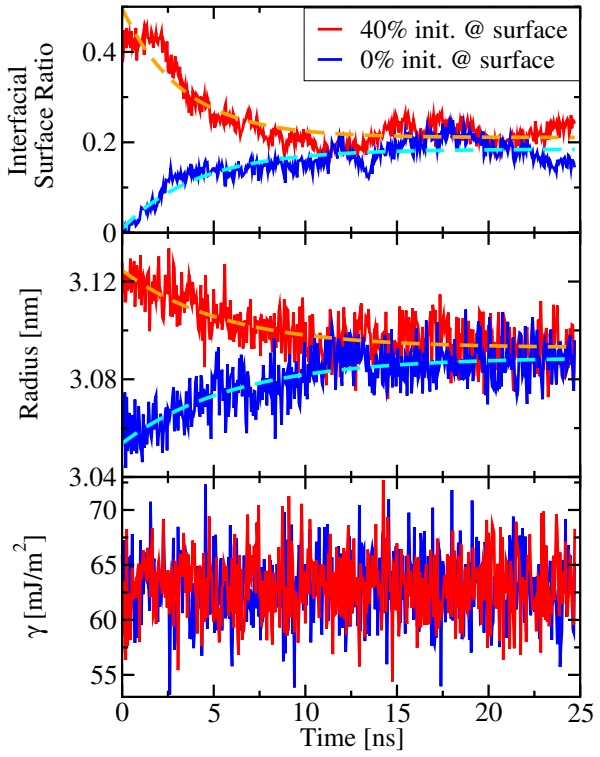

Figure 3: Time-dependent properties of a thermodynamically stable bubble with $L = 16$ nm and $R/L \approx 0.15$ and a CG surfactant:water ratio of 1:1,000 initialized with an interfacial surfactant ratio of either 40% (red) or 0% (blue). At equilibrium, these correspond to mole fractions of surfactant in the bulk of $(8.2 \pm 0.4) \times 10^{-4}$. Time dependence of (Top) the fraction of interfacial surfactants, as measured by integrating from $r_1 - 2\sigma$ to $r_1 + 2\sigma$; (Middle) the bubble radius; and (Bottom) the surface tension. In the Top and Middle panels, fit functions of the form $A\exp(-r/\tau) + C$ are plotted to extract decay constants, τ.

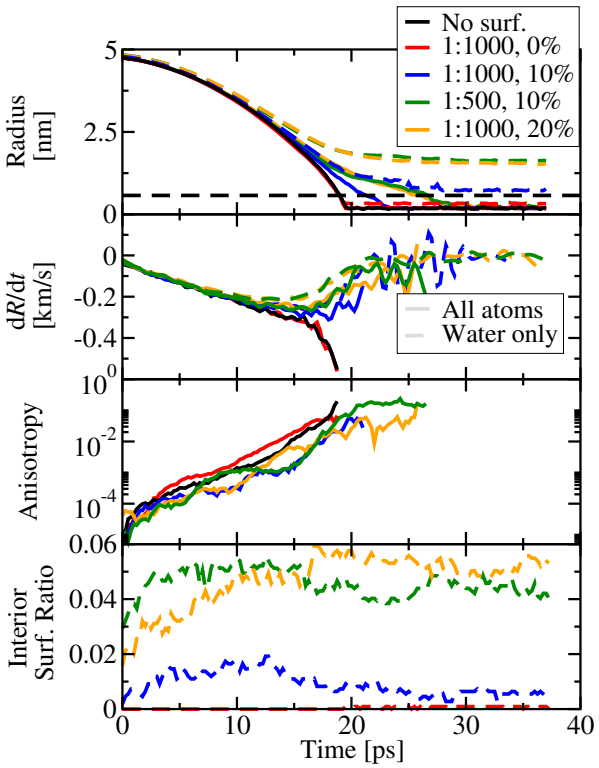

Figure 4: Bubble collapse metrics obtained with the CG model for $L = 32$ nm and $R/L = 0.15$ systems containing no surfactant or surfactant:water molar ratios of 1:1,000 or 1:500. Initial interfacial surfactant ratios are 0, 10, or 20%. (Top) Bubble radius, as defined using water molecules only (dashed lines) or water and surfactant molecules both (solid lines). A dotted horizontal line differentiates bubbles larger than those that arise spontaneously due to thermodynamic fluctuations. (Top Middle) Derivatives of bubble radius with respect to time. With interfacial surfactant, an inflection point in $R(t)$ is observed. (Bottom Middle) Anisotropy κ, measured using the all-atom bubble detection criterion. (Bottom) The interior surfactant ratio, $N^{\text{inside}}_{\text{surfactant}}/N_{\text{surfactant}}$, with $N^{\text{inside}}_{\text{surfactant}}$ defined as the number of surfactant molecules within the bubble as measured from water only.

liquid is on the order of nanoseconds, collapse for sub-10 nm bubbles tends to occur on the scale of tens of picoseconds, with precise collapse times dependent on the initial R/L value (that controls the volume occupied by the bubble and, hence, the compression and initial pressure for the surrounding liquid), the system size, and the interfacial surfactant concentration (see Figure 4).

Bubble collapse dynamics reveal that increasing the initial interfacial surfactant ratio leads to a longer collapse time associated with a decrease in the surface tension (see Figure 4, Top). Interestingly, the concentration of surfactant in the bulk plays a less important role on the behavior of $R(t)$, presumably because it affects only marginally the viscosity of the surrounding liquid. This can be seen when comparing simulations with surfactant:water mole ratios that differ by a factor of two (1:1,000 and 1:500) and interfacial surfactant ratios that differ by a compensatory factor of two (20% and 10%, respectively), in which the number of surfactant molecules at the interface are identical but the concentration of surfactant in the bulk solution is changed. These two simulation conditions give nearly identical behaviors of $R(t)$.

An inflection point in the $R(t)$ profile appears when the initial interfacial surfactant concentration is nonzero, as indicated by a local minimum in dR/dt for all cases where the bubble interface is enriched (Figure 4,

Top Middle). This behavior is reflected in the RP analysis (see below). As bubble collapse proceeds, the bubble tends to become less spherical regardless of whether surfactant is present at the interface or not (Figure 4, Bottom Middle). This is attributed to the increasing importance of molecular detail at small length scales, where a continuum description of the bubble is not appropriate. This indicates that radii reported become less accurate as time proceeds due to the assumption of sphericity breaking down.

The bubble detection algorithm used here was originally formulated for a one-component liquid–vapor interface. This method provides different results when applied to bubble collapse when gas molecules (Siepmann *et al.*, 2020) or surfactant are present (i.e., two-component systems) depending on which atoms are provided as inputs to the bubble detection algorithm. When all atom types are used to determine regions of space that are excluded from the bubble, then the bubble radius is found to decay to below the threshold of thermodynamic fluctuations within less than 30 ps in all cases for the CG model and system size $L = 32$ nm and $R/L = 0.15$ (see Figure 4, Top, solid lines). However, when only water molecules are used in the bubble detection algorithm, the bubble radius can be seen to plateau at large radii for the simulations with initial non-zero interfacial surfactant fraction (Figure 4, Top, dashed lines).

The difference between these two estimates for $R(t)$ is caused by the slow dissolution dynamics for surfactants that lags behind the bubble collapse dynamics. Thus, the surfactant molecules becoming enriched at the innermost liquid shell as the volume and surface area decrease rapidly. Using the bubble radius as defined by detecting only water molecules, the number of surfactant molecules contained within this volume is reported in Figure 4, Bottom, normalized by the total number of surfactant molecules ($N^{\text{inside}}_{\text{surfactant}}/N_{\text{surfactant}}$).

During the initial, slower stage of the bubble collapse, this ratio is found to increase somewhat. The increase appears to originate from some surfactant molecules that were initially buried slightly deeper in the interface and are pushed toward the bubble interior as the surface area decreases. More importantly, beyond this initial phase, the number of surfactant molecules remains remarkably constant despite that the bubble volume decrease by an order of magnitude or more. For the two simulations with the non-zero initial interfacial surfactant population, we observe the formation of a surfactant droplet (see Figure 5). It appears that this bubble is depleted in water molecules beyond what would be expected of the organic-rich phase of the immiscible water/pentan-3-ol mixture.

The surfactant density enhancement is attributed to confinement effects during bubble collapse, drawing an essentially fixed number of surfactant molecules into an ever-smaller region as the bubble radius decreases. This effect is particularly striking in the extent to which it effects pentan-3-ol more than water. The radial density profile of water, $\rho_{\text{w}}(t)$, sees a departure from its equilibrium sigmoid character (see Figure 6, Top) with a long tail in toward the bubble center. In contrast, the density profile of pentan-3-ol, $\rho_{\text{s}}(t)$, is peaked close to the bubble center and its long tail

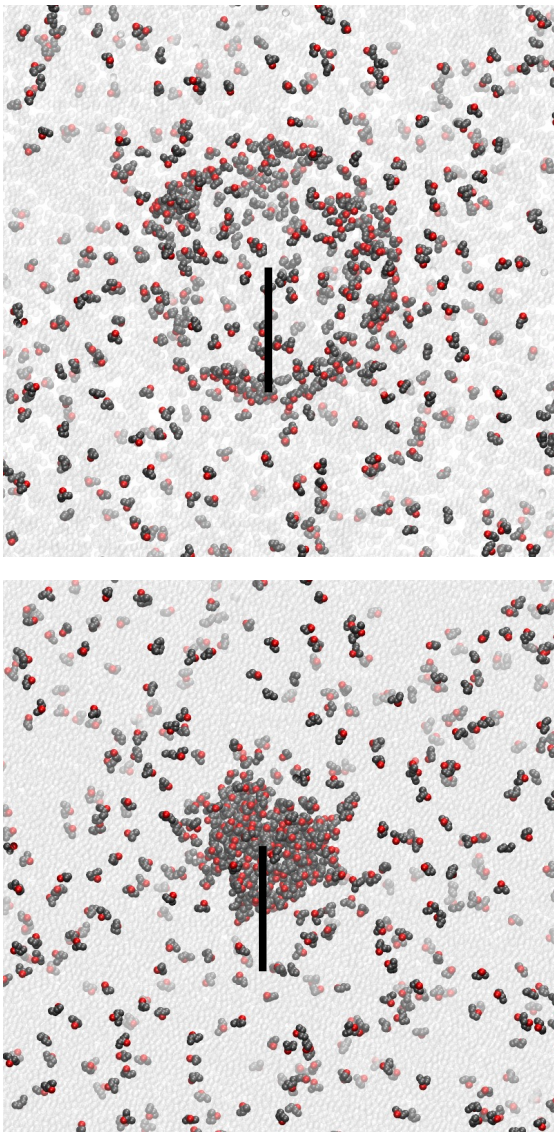

Figure 5: Representative simulation snapshots illustrating surfactant localization at the beginning ($t = 0$ ps, Top) and end ($t = 30$ ps, Bottom) of bubble collapse for the CG system with $L = 32$ nm, $R/L = 0.15$ containing a surfactant:water mole ratio of 1:1,000 and an initial interfacial surfactant fraction of 20%. By $t = 30$ ps, no vacuous bubble remains, but a large surfactant aggregate is prominent. The scale bar in both panels is equivalent to 4.75 nm ($= R_0$).

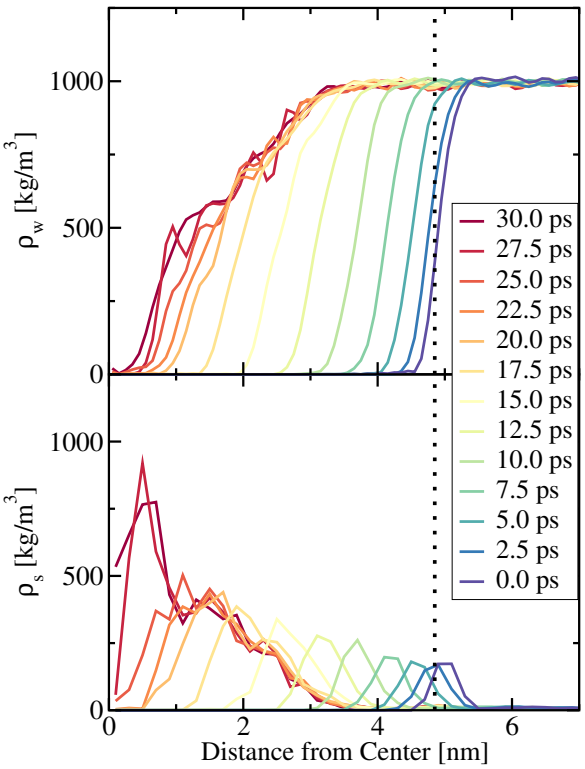

Figure 6: Mass density of CG water (Top) and pentan-3-ol (Bottom) as a function of distance from the cavity center and time, during the collapse of a bubble with $L = 32$ nm and $R/L = 0.15$ containing a surfactant:water mole ratio of 1:1,000 and an initial interfacial surfactant ratio of 20%. The black dashed line indicates the bubble radius at time $t = 0$ ps.

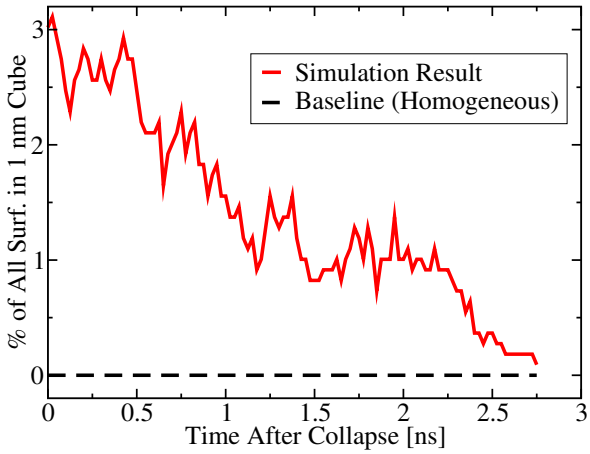

Figure 7: Percentage of all surfactant molecules within a $1\times1\times1$ nm^3 cube that contains the highest concentration of surfactant. Prior to bubble collapse, with $L = 32$ nm and $R/L = 0.15$ and overall surfactant:water mole ratio 1:1,000, the interfacial surfactant ratio was 20%. The baseline assumes a homogeneous surfactant distribution, using the volume fraction of the region ($1/32^3 \approx 3\times10^{-5}$).

extends away from the bubble center (Figure 6, Bottom). As the total surface area of the bubble decreases during collapse, surfactant molecules out-compete water for space at the interface. It is also apparent from Figure 6 that the interfacial width increases, as both $\rho_w(t)$ and $\rho_s(t)$ appear to broaden with time. This observation should be treated cautiously, however, because as seen in Figure 4 (Bottom Middle) the bubble becomes less spherical at small radii and therefore a radial analysis does not accurately capture the complex morphology of the bubble.

Following bubble collapse, this surfactant aggregate persists in solution for nanoseconds. A $1\times1\times1$ nm^3 region that contains the highest concentration of surfactant contains more than 3% of all surfactant molecules immediately after bubble collapse, nearly three orders of magnitude higher than would be expected from a homogeneous distribution of surfactant in that same volume fraction (see Figure 7). The pentan-3-ol within this cube remains above its homogeneously dispersed concentration for several nanoseconds, meaning that the collapse of a surfactant-rich bubble gives rise to locally surfactant-enriched regions of space on time scales that far exceed bubble collapse itself.

Finally, bubble collapse dynamics can be compared agains the RP equation, which is first discussed using the CG model for an $L = 32$ nm and $R/L = 0.15$ system. One of the inputs for the RP equation is a time-dependent pressure, $\Delta P(t)$, which here is taken as the simulation virial pressure. Representative traces are plotted in Figure 8. Interestingly, at the two highest surfactant concentrations used here (surfactant:water mole ratios 1:500 and 1:1,000 and interfacial surfactant ratios 10% and 20%, respectively), the amount of surfactant present is insufficient to change the virial pressure compared to the surfactant-free condition.

In order to achieve atmospheric pressure at equilibrium, the initial pressure is large due to the liquid being slightly compressed (by about 1.5%). The behavior of the virial pressure is indistinguishable in the three traces. In each case these are smoothed via cubic splines for use as an input to the RP equation as $\Delta P(t)$. Therefore, differences in collapse dynamics are largely attributed to the effective interfacial surface tension γ, and to a lesser extent the kinematic viscosity ν_S, which deviates by a smaller relative extent between the systems considered here. Agreement between the RP equation and simulation results is expected to persist over a diversity of initial conditions and driving pressures, although further study is needed to identify the ramifications of parameters like external pressure on effective quantities, such as γ.

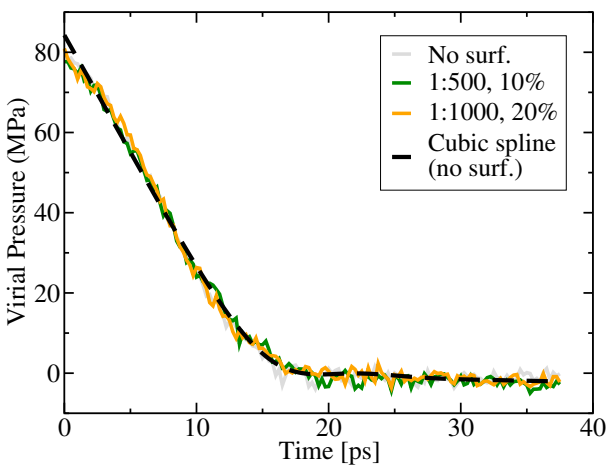

Figure 8: Simulation virial pressures as a function of time during bubble collapse for $L = 32$ nm and $R/L = 0.15$ for CG systems that contain no surfactant (water only), gray, and two that contain pentan-3-ol at surfactant:water molar ratios of 1:500 (green) and 1:1,000 (gold). No substantive deviations are shown in the time-dependent pressure profiles at these molar ratios. To supply this pressure data to numerical RP implementations, data was smoothed using a cubic spline as illustrated in black dashes for the no surfactant condition.

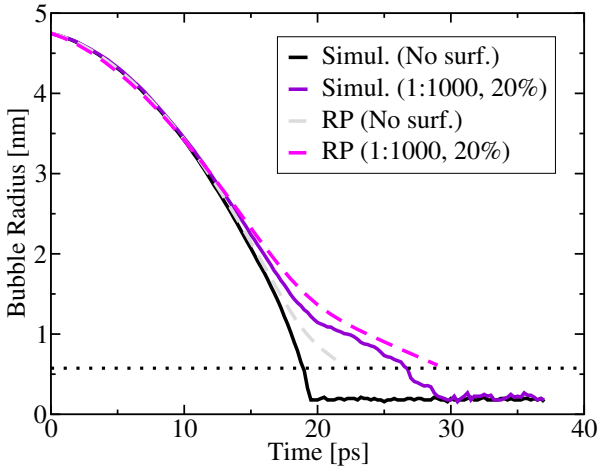

Figure 9: Comparison of simulated (solid line) bubble collapse radius ($L = 32$ nm, $R/L = .15$, CG model) to the Rayleigh-Plesset equation (dashed line), using no surfactant (black) or at a ratio of 1:1,000 with water (purple), with an initial interfacial surfactant ratio of 20%. The RP solution to the no surfactant condition utilized parameters $\gamma = 66$ mN/m and $\nu_S = 3.17 \times 10^{-7}$ m^2/s, while with 1:1,000 surfactant these values were $\gamma =$ 45 mN/m and $\nu_S = 3.3 \cdot 10^{-7}$ m^2/s.

Agreement between simulation trajectories and RP calculations are generally satisfactory when using a time-independent effective γ. Since the interfacial concentration of pentan-3-ol changes as a function of time, the effective γ used must be a compromise over the actual $\gamma(t)$ throughout the collapse. When no surfactant is present, bubble collapse can be modeled remarkably well using values for γ and ν_S measured in simulation (66 mJ/m^2 and 3.17×10^{-7} m^2/s, respectively) (see Figure 9).

The success of the RP equation in matching simulation data from time-independent γ and ν_S is to some extent expected. In the case of γ, the surface tension is rather robust as a function of bubble radius when measured from thermodynamically stable bubbles. Chen *et al.* (2019) showed that for bubble radii varying from ~1 to 10 nm, γ varies by $< 20\%$. For ν_S, the volume fraction of bulk-like liquid far exceeds the maximum bubble volume V_b (V_b/L^3 = 0.0141), and so the equilibrium value of ν_S at a given bulk surfactant concentration is well-representative of the solution far from the bubble wall throughout the collapse. While viscosity is in general a pressure-dependent quantity, experimental results in liquid water suggest the fractional change in ν_S may also be small (Schmelzer *et al.*, 2005).

When surfactant is present, the effective γ required to reproduce simulation data plummets. For the system containing a surfactant:water mole ratio of 1:1,000 with an initial interfacial surfactant ratio of 20%, the corresponding mole fraction of surfactant in the bulk is near 8×10^{-4}. Based upon equilibrium surface tensions at the planar interface, γ is expected to be near that of neat water, in the vicinity of 66 mN/m. Here, however, the RP equation requires an effective γ of only 45 mN/m to reproduce simulation results (see Figure 9). Although low, this value is well above that for the liquid-vapor interface of neat pentan-3-ol. In this scenario, where the interfacial concentration of pentan-3-ol increases with time, γ is truly time-dependent, and so the effective γ used in the RP model must be a compromise over the collapse duration. While it remains unclear how the correct effective γ should be estimated for a surfactant-rich system *a priori*, it is remarkable that such close agreement can be obtained without explicitly modeling $\gamma(t)$. This suggests that RP-based models can be extended to include surfactant-rich systems without necessitating dynamic variables if the relationship between effective surface tension and system descriptors (e.g., surfactant concentration or external pressure) can be deduced. Therefore, nanoscopic parameters such as surface dynamics can be accounted for within the macroscopic model.

Thus far, the discussion has been largely focused on the computationally inexpensive CG model. We now turn to a comparison between the CG and MM models during bubble collapse. For this, a slightly smaller system size of $L = 16$ nm and $R/L = 0.15$ is used, following the

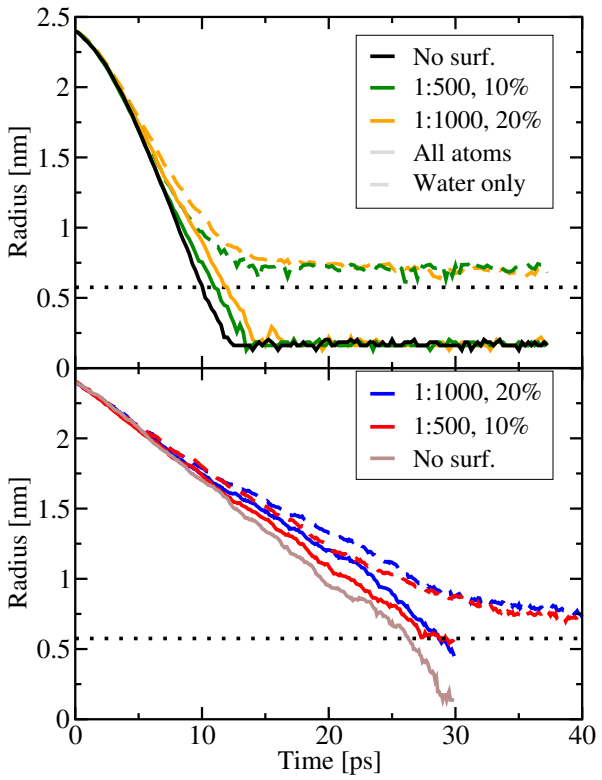

Figure 10: Bubble collapse radii for $L = 16$ nm and $R/L = 0.15$ systems containing no surfactant or surfactant:water mole ratios of 1:500 or 1:1,000. The initial interfacial surfactant ratios were 10% and 20%, respectively. (Top, Bottom) Bubble radii for CG and MM systems, respectively, as defined using water molecules only (dashed lines) or all atoms (solid lines), as in Figure 4.

same collapse protocol as above, and $R(t)$ is monitored as a function of time using the two different bubble detection criteria as before (see Figure 10). In agreement with previous reports (Siepmann *et al.*, 2020), the significantly higher (and more accurate) shear viscosity for the MM model leads to slowed collapse dynamics compared to the CG model under all conditions examined. Notably, at the relatively small system size used here, the impacts of included surfactant are diminished because the absolute number of surfactants placed initially at the interface is eight times smaller when the boxlength is halved. For $L = 16$ nm, both models display little curvature in $R(t)$ and do not have obvious inflection points. A commonality between the system sizes and models used is that an aggregate of pentan-3-ol persists in solution immediately following bubble collapse, as can be seen when comparing bubble detection methods (compare dashed vs. solid lines in Figure 10). The size of this aggregate is clearly related the total number of surfactant molecules that begin on the bubble surface, as the CG and MM models predict aggregates of similar radii, which are both smaller than shown for the CG model in the $L = 32$ nm scenario. These data suggest, however, that such an enrichment of pentan-3-ol occurs during bubble collapse when surfactant is present at the interface well below the saturation limit.

CONCLUSION

The molecular simulations shown here provide information on the thermophysical impact of surfactants on bubble collapse dynamics. The most pronounced ramifications for CFD simulations relate to the time scales of surfactant localization. For a thermodynamically stable bubble that persists over long times but is initialized with a non-equilibrium surface concentration of pentan-3-ol, molecular simulations indicate that several nanoseconds may be required for surfactants to re-distribute between interface and surrounding region and for (local) equilibrium to be reached. This is in contrast to the time scales of bubble collapse, which are 2-3 orders of magnitude faster. We surmise that this problem of disparate time scales also persists during the collapse of macroscopic bubbles with initial radii on the micron scale. Once the rapid phase of the collapse starts, surfactant molecules are "trapped".

Furthermore, this work reveals that the equilibrium surface concentrations of pentan-3-ol differ depending upon bubble curvature, with tighter curvatures disfavoring surfactant adsorption due to the more favorable hydrogen bond network that may be formed around a convex surface (compared to a planar one). This effect diminishes in intensity as the bubble radius far exceeds one nanometer.

During bubble collapse, the surface concentration of surfactant enriches with time as the bubble surface area decreases while the number of surfactant molecules remains largely unchanged, since the innermost liquid shell is composed of nearly pure surfactant. This has two ramifications: Firstly, the changing interfacial concentration corresponds to a dramatic change in surface tension, γ, over time. Remarkably, the bubble dynamics can be captured well by a single effective value of γ, although the value this parameter should take is not clear *a priori*. Secondly, after the collapse, the droplet formed by the excess surfactant molecules is fairly long lived and may act as nucleation site for future bubble formation. In contrast to the gas bubble collapse, the dense surfactant droplet does not trigger an immediate bubble rebound.

The disparate time scales for bubble collapse and surfactant dissolution indicate that the assumptions of instantaneous equilibrium that are included in many CFD models must be treated with caution. Future molecular simulation studies should be aimed at elucidating

finite-size effects and model dependence on the physical phenomena described here. Particularly, the time to equilibrate surfactant with the bubble interface is expected to increase as the total surface area becomes larger, and post-collapse surfactant aggregates will persist for longer durations as the total number of molecules in the cluster increases. It is desirable to further connect with CFD simulations and identify the significance of these effects in turbulent flows and whether surfactant localization tendencies on the nanosecond time scale are impactful for large-scale bubble dynamics. Further connections are practically attainable for systems that include multiple bubbles and spanning a range of nanoscopic length scales, but outstanding challenges remain in describing turbulent flows across intermediate spatiotemporal scales that are too small for CFD and too large for MD. In these instances, a transitional approach is unavailable and the gap must be bridged by addressing trends in system size at the spatiotemporal limits accessible to these existing schemes.

ACKNOWLEDGEMENTS

This work was supported by the Unites States Office of Naval Research under Grant ONR N00014-17-1-2676 with Dr. Ki-Han Kim as the program manager. Part of the computer resources was provided by the Minnesota Supercomputing Institute.

REFERENCES

Abascal, J. L. F. and Vega, C., "A general purpose model for the condensed phase of water: TIP4P/2005," Journal of Chemical Physics, Vol. 123, 2005, pp. 234505.

Allen, M. P. and Tildesley, D. J., Computer simulation of liquids, Oxford University Press, Inc., 1987.

Bevington, P. R. and Robinson, D. K., Data reduction and error analysis, McGraw-Hill, Inc., 2003.

Bhatt, M. and Mahesh, K., "A numerical approach to address the acoustic stiffness in cavitating flows," International Journal of Multiphase Flow, Vol. 141, 2021, pp. 103568.

Cahn, J. W. and Hilliard, J. E., "Free energy of a nonuniform system. I. Interfacial free energy," Journal of Chemical Physics, Vol. 28, 1958, pp. 258-267.

Campañá, C. and Miller, R. E., "Physical properties of liquid hexane and derived polar by-products of hexane autoxidation: molecular dynamics calculations using the TraPPE-UA force field," Molecular Simulation, Vol. 39, 2013, pp. 882-894.

Chandler, D., "Interfaces and the driving force of hydrophobic assembly," Nature, Vol. 437, 2005, pp. 640-647.

Chen, B., Potoff, J. J., and Siepmann, J. I., "Monte Carlo calculations for alcohols and their mixtures with alkanes. Transferable potentials for phase equilibria. 5. United-atom description of primary, secondary, and tertiary alcohols," Journal of Physical Chemistry B, Vol. 105, 2001, pp. 3093-4104.

Chen, B., Siepmann, J. I., and Klein, M. L., "Vapor–liquid interfacial properties of mutually saturated water/1-butanol solutions," Journal of the American Chemistry Society, Vol. 124, 2001, pp. 12232-12237.

Chen, J. L., Xue, B., Mahesh, K., and Siepmann, J. I., "Molecular simulations probing the thermophysical properties of homogeneously stretched and bubbly water systems," Journal of Chemical Engineering & Data, Vol. 64, 2019, pp. 3755-3771.

Crowe, C. T., Multiphase flow handbook, CRC Press, Inc., 2005.

Custer, G. S., Xu, H., Matysiak, S., and Das, P., "How hydrophobic hydration destabilizes surfactant micelles at low temperature: a coarse-grained simulation study," Langmuir, Vol. 34, 2018, pp. 12590-12599.

Grunberg, L. and Nissan, A. H., "Mixture law for viscosity," Nature, Vol. 164, 1949, pp. 799-800.

Kelkar, M. S., Rafferty, J. L.; Siepmann, J. I., and Maginn, E. J., "Prediction of viscosities and vapor–liquid rquilibria for five polyhydric alcohols by molecular simulation," Fluid Phase Equilibria, Vol. 260, 2007, pp. 218-231.

Kirkwood, J. G. and Buff, F. P., "The statistical mechanical theory of surface tension," Journal of Chemical Physics, Vol. 13, 1949, pp. 338-343.

Kubo, R., "Statistical-mechanical theory of irreversible processes. I. General theory and simple applications to magnetic and conduction problems," Journal of the Physical Society of Japan, Vol. 12, 1957, pp. 570-586.

Luo, X. W., Ji, B., and Tsujimoto, Y., "A review of cavitation in hydraulic machinery," Journal of Hydrodynamics, Vol. 28, 2016, pp. 335-358.

Martínez, L., Andrada, R., Birgin, E. G., and Martínez, J. M., "PACKMOL: a package for building initial configurations for molecular dynamics simulations," Journal of Computational Chemistry, Vol. 30, 2009, pp. 2157-2164.

Molinero, V. and Moore, E. B., "Water modeled as an intermediate element between carbon and silicon," Journal of Physical Chemistry B, Vol. 113, 2009, pp. 4008-4016.

Muradoglu, M. and Tryggvason, G., "Simulations of soluble surfactants in 3D multiphase flow," Journal of Computational Physics, Vol. 274, 2014, pp. 737-757.

Ryckaert, J. P., Ciccotti, G., and Berendsen, H. J., "Numerical integration of the cartesian equations of motion of a system with constraints: molecular dynamics of n-alkanes," Journal of Computational Physics, Vol. 23, 1977, pp. 327-341.

Sabbaghzadeh, B., Upstill-Goddard, R. C., Beale, R., Pereira, R., and Nightingale, P. D., "The Atlantic Ocean surface microlayer from 50 °N to 50 °S is ubiquitously enriched in surfactants at wind speeds up to 13 m s^{-1}," Geophysical Research Letters, Vol. 44, 2017, pp. 2852-2858.

Schmidmayer, K., Bryngelson, S. H., and Colonius, T., "An assessment of multicomponent flow models and interface capturing schemes for spherical bubble dynamics," Journal of Computational Physics, Vol. 401, 2020, pp. 109080.

Siepmann, J. I., Chen, J. L., Liang, B., and Mahesh, K., "Effect of non-condensable gas on the thermophysical properties of bubbly water and on bubble collapse dynamics probed by molecular simulations," 33rd Symposium on Naval Hydrodynamics, Osaka, Japan.

Schmelzer, J. W., Zanotto, E. D., and Fokin, V. M., "Pressure dependence of viscosity," Journal of Chemical Physics, Vol. 122, 2005, pp. 074511.

Stillinger, J. F. H., "Rigorous basis of the Frenkel-Band theory of association equilibrium," Journal of Chemical Physics, Vol. 38, 1963, pp. 1486-1494.

Takagi, S. and Matsumoto, Y, "Surfactant effects on bubble motion and bubbly flows," Annual Review of Fluid Mechanics, Vol. 43, 2011, pp. 615-636.

Thompson, A. P., Aktulga, H. M., Berger, R., Bolintineanu, D. S., Brown, W. M., Crozier, P. S., in't Veld, P. J., Kohlmeyer, A., Moore, S. G., Nguyen, T. D., Shan, R., Stevens, M. J., Tranchida, J., Trott, C., and Plimpton, S. J., "LAMMPS - a flexible simulation tool for particle-based materials modeling at the atomic, meso, and continuum scales," Computer Physics Communications, Vol. 271, 2022, pp. 10817.

Vargaftik, N. B., Volkov, B. N., and Voljak, L. D., "International tables of the surface tension of water," Journal of Physical and Chemical Reference Data, Vol. 12, 1983, pp. 817-820.

Vega, C. and De Miguel, E., "Surface tension of the most popular models of water by using the test-area simulation method," Journal of Chemical Physics, Vol. 126, 2007, pp. 154707.

Yadigaroglu, G. and Hewitt, G. F., Introduction to multiphase flow: basic concepts, applications and modelling, Springer Press, Inc., 2017.

Zhang, Y., Otani, A., and Maginn, E. J., "Reliable viscosity calculation from equilibrium molecular dynamics simulations: A time decomposition method," Journal of Chemical Theory and Computation, Vol. 11, 2015, pp. 3537-3546.